



# CHORUS

This is the accepted manuscript made available via CHORUS. The article has been published as:

## Effect of Laser-Matter Interaction on Molten Pool Flow and Keyhole Dynamics

Nadia Kouraytem, Xuxiao Li, Ross Cunningham, Cang Zhao, Niranjana Parab, Tao Sun, Anthony D. Rollett, Ashley D. Spear, and Wenda Tan

Phys. Rev. Applied **11**, 064054 — Published 24 June 2019

DOI: [10.1103/PhysRevApplied.11.064054](https://doi.org/10.1103/PhysRevApplied.11.064054)

# Effect of laser-matter interaction on molten pool flow and keyhole dynamics

Nadia Kouraytem<sup>a</sup>, Xuxiao Li<sup>a</sup>, Ross Cunningham<sup>b</sup>, Cang Zhao<sup>c</sup>, Niranjana Parab<sup>c</sup>, Tao Sun<sup>c</sup>, Anthony D. Rollett<sup>b</sup>, Ashley D. Spear<sup>a</sup>, Wenda Tan<sup>a,\*</sup>

<sup>a</sup>Department of Mechanical Engineering, The University of Utah, Salt Lake City, Utah 84112, USA

<sup>b</sup>Department of Materials Science and Engineering, Carnegie Mellon University, Pittsburgh, Pennsylvania 15213, USA

<sup>c</sup>X-ray Science Division, Advanced Photon Source, Argonne National Laboratory, Lemont, Illinois 60439, USA

## Abstract

Laser-induced keyholing occurs in additive manufacturing and welding processes, but the keyhole dynamics have not been well understood. A multi-phase and multi-physics numerical model is used to predict the keyhole shapes recorded in the experimental observations and to predict transient and non-uniform distributions of laser absorption, temperature, and flow velocity in the process. When compared against data from a state-of-the-art dynamic X-ray radiography technique, good agreement is found for the keyhole shapes and fluctuation of the gas-liquid interface, thereby validating the simulation method. A detailed discussion is then given to elucidate the effects of laser absorption on the dynamic behavior of the front and rear keyhole walls. A quantitative comparison of different driving forces on the keyhole is also given to evaluate their significance to the keyhole dynamics.

**keywords** laser material processing, laser absorption, keyhole dynamics, x-ray radiography, multi-physics modeling

## 1. Introduction

The keyholing phenomenon is frequently found in laser-based metal additive manufacturing and welding processes. As shown in Fig. 1, a keyhole starts with a laser of an adequately high power intensity that induces not only melting but also surface evaporation of the metals. The high-speed flow of evaporated metal (denoted by the purple arrows) exerts a recoil pressure on the molten pool surface, which pushes the molten metal aside to create a keyhole. The gas-liquid interface of the keyhole usually exhibits strong fluctuations, which is found to be the major reason for the formation of spatters and pores [1, 2, 3, 4]. The detailed fluctuation dynamics of laser-induced keyholes are complex and not fully understood. Extensive experimental and modeling efforts have been focused to investigate this issue.

The experimental investigations of keyhole dynamics are primarily through visualization of the keyhole shape. Optical imaging has been used most frequently to observe the keyhole dynamics from the top-view [3, 5, 6, 7, 8] and side-view [9, 10, 11]. Alternatively, X-ray imaging provides a unique capability to penetrate non-destructively opaque metals for in-situ observation of keyhole dynamics without disturbing the process [1, 2, 4, 12, 13, 14, 15, 16, 17]. These visualization-based works have collectively disclosed that the keyhole adopts different shapes as a function of power and speed and its internal surface generally fluctuates noticeably. The shape and fluctuation magnitude and frequency are affected by a variety of factors, including laser parameters (laser power, scanning speed,

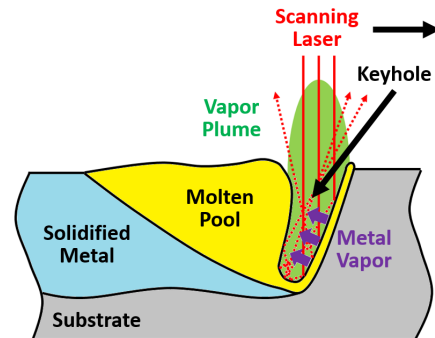


Figure 1: Schematic of laser-induced keyhole.

pulse width and duty cycle, etc.), protective gas environment, and properties of substrate metals.

Since the absorbed laser light is the dominant energy source that induces keyhole formation, it is critical to measure the laser absorption by the keyhole. The measurements using calorimetry [18, 19] or the integrated sphere method [20] have clearly revealed that the total laser absorption is noticeably increased when a keyhole is formed and that the increment in absorptivity is highly dependent on the keyhole geometry. This originates in the multiple-reflection phenomenon of the laser light inside the keyhole. The integrated sphere method can also capture the dynamic fluctuation of laser absorption [20], which is attributed to the dynamic fluctuation of keyhole geometry.

Despite the significant advancement in experimental observation of keyhole dynamics, important information regarding keyhole dynamics is still missing. First, the current techniques

\*corresponding author: wenda.tan@mech.utah.edu

cannot measure the spatial distribution of the laser absorption on the keyhole wall, which is expected to be non-uniform and has decisive effects on the keyhole dynamics. Furthermore, the keyhole evolution is closely coupled with the metal evaporation and thermofluidic flows of the liquid/vapor metals, both of which are difficult to measure through experimentation, especially when the metals are in a high-temperature and dynamic state. Without the above information, it is infeasible to obtain a complete understanding of the keyhole dynamics.

Numerical modeling complements experiments and enhances the understanding of keyhole dynamics by providing information that is difficult to measure with experiments. Ray-tracing models are widely used to simulate the multiple reflections and partial absorption of laser light inside the keyhole. The models can successfully predict the non-uniform laser absorption in keyhole of different shapes [21, 22, 23, 24, 25, 26] and have well demonstrated that the laser absorption is highly dependent on the keyhole shape. In the more recent multi-physics modeling of keyhole dynamics [27, 28, 29, 30, 31, 32, 33, 34, 35, 36, 37, 38, 39], the ray tracing model is coupled with a computational thermofluidic dynamics model and a free surface tracking model (based on level-set, volume-of-fluid, or arbitrary Lagrangian-Eulerian methods). The ray tracing model can predict the distribution of laser absorption intensity on the keyhole wall, which is used in the thermofluidic model to drive the variations of temperature field and fluid flow in both the molten pool and surrounding gaseous region. The predicted flow velocity will inform the surface tracking model, which updates the location of the metal surface, a part of which is the keyhole wall. While these multi-physics models have already been used to investigate various issues regarding the formation and dynamic evolution of laser-induced keyholes, their predictions of the keyhole shape and fluctuation have rarely been validated against physical measurements of real keyholes. Hence, the quantitative accuracy of the simulations is still not clear.

In this paper, we present a combination of the state-of-the-art dynamic X-ray radiography (DXR) experimental measurements with an in-house multi-physics numerical model to investigate the dynamic phenomena of laser-induced keyholes in stainless steel (SS) 304. The DXR system at the Advanced Photon Source (APS) is first used to perform in-situ observation of the keyhole dynamics for a wide range of laser power and scanning speed. The multi-physics model is then used to simulate the 3-dimensional (3D) dynamic keyhole phenomenon. The model can well replicate the keyhole shape and fluctuation observed in the DXR experiments, and the simulation results are further leveraged to understand the effects of non-uniform laser absorption on temperature and flow fields of the liquid/vapor metals as well as the dynamic keyhole behavior.

## 2. Results

### 2.1. Dynamic X-ray radiography experiments

In our DXR experiments, a high energy, high flux X-ray beam penetrated through the opaque metal substrate to image the keyhole shape with high spatial and temporal resolutions

(see Appendix A for the details). The typical keyhole shapes generated by different laser powers and scanning speeds are shown in Fig. 2. To quantify the keyhole shape, we schematically define the local keyhole depth  $d_k$ , local keyhole width  $w_k$ , and local front keyhole wall inclination  $\alpha$  in the insert of Fig. 2. Here, we define the keyhole width as the horizontal distance between the front and rear keyhole wall at mid-depth.

The effects of laser scanning speed were investigated as a series of experiments at constant laser power  $P = 416$  W. With increasing laser scanning speed ( $V = 300 - 1200$  mm/s), the keyhole depth decreases from around  $370 \mu\text{m}$  to around  $118 \mu\text{m}$ , and the front wall inclination  $\alpha$  increases from around  $9^\circ$  to  $47^\circ$ . These trends are consistent with those reported in [5]. The keyhole width varies along the depth direction in all cases. When the laser scanning speed is  $\leq 400$  mm/s, the keyhole is generally wider at the lower portion than on the upper portion. As the scanning speed is increased to be  $\geq 600$  mm/s, the upper portion of the keyhole becomes wider than the lower portion. Three typical cases were selected from this series (case 1 in the red box, case 2 in the blue box, and case 3 in green box in Fig. 2) for direct comparison with numerical simulation. In case 1, with the combination of high laser power of  $P = 416$  W and low scanning speed of  $V = 300$  mm/s, the keyhole presents the traditional deep and slender shape. As the scanning speed increases in case 2 to  $V = 400$  mm/s, the keyhole becomes shallower and wider, presenting a quasi-quadrilateral shape. A further increase of the scanning speed to  $V = 800$  mm/s in the green case 3 changes the keyhole to a triangular shape.

Varying the laser power was investigated at a constant scanning speed of  $V = 600$  mm/s. As the laser power increases from 208 to 416 W, the keyhole depth increases from about  $55$  to  $129 \mu\text{m}$ , the front wall inclination decreases from around  $45^\circ$  to  $34^\circ$ , the keyhole width at half depth increases from around  $68$  to  $155 \mu\text{m}$ , and similarly the keyhole width at the top surface increases from about  $102$  to  $220 \mu\text{m}$ .

While the front keyhole wall is generally stable, which leads to relatively constant keyhole depth and front-wall inclination, the rear keyhole wall continuously changes its shape and relative location with respect to the front wall. Since the keyhole width is not uniform along the keyhole depth direction, we quantify the general keyhole width with its value at half of the keyhole depth, and plot, in Fig. 3, the temporal variation of the keyhole width for the three typical cases. The average keyhole width is the minimum for case 1 of  $P = 416$  W and  $V = 300$  mm/s ( $73 \mu\text{m}$ ), indicating that the keyhole is rather narrow when the laser scanning speed is low. With the scanning speed increased to  $V = 400$  mm/s and  $V = 800$  mm/s, the average keyhole width is noticeably increased in case 2 ( $120 \mu\text{m}$ ) and case 3 ( $107 \mu\text{m}$ ).

As the keyhole continuously changes its width around the average value, we quantify the fluctuation of keyhole width by its magnitude and period. The fluctuation magnitude is defined as the difference between the maximum and minimum width in each case, and is found to decrease as the laser scanning speed increases from case 1 to case 3 ( $85 \mu\text{m}$ ,  $61 \mu\text{m}$ , and  $25 \mu\text{m}$ , as delineated by the colored double-headed arrows in Fig. 3). The fluctuation period is defined as the time difference between

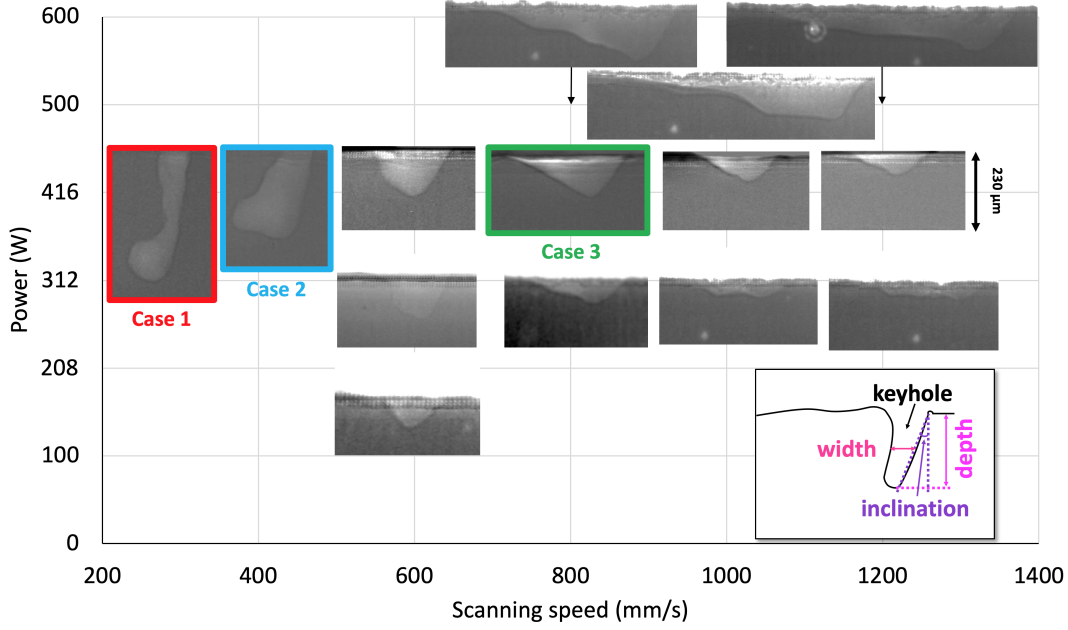


Figure 2: Keyhole processing map for SS304 with different laser powers and scanning speeds. The colored boxes highlight the three selected cases of typical keyhole shapes for further investigation. For all three cases the experiments were performed at the same laser power  $P = 416$  W and varying scanning speeds: Case 1 at  $V = 300$  mm/s; Case 2 at  $V = 400$  mm/s; Case at 3  $V = 800$  mm/s. The inset sketch defines the geometrical parameters used in the course of the study.

two adjacent moments when the instantaneous keyhole width decreases from above to below the average value, and is found to be around  $100 \mu s$  in all the three cases. This corresponds to a fluctuation frequency of around 10 kHz, which is of the same magnitude as the previous experimental measurements based on acoustic and optical signals [40, 41, 42]. Note that the frequency of 10 kHz primarily describes the fluctuation of the entire keyhole. Local fluctuation with higher frequencies are found at different locations and instances on the keyhole wall but the length scale and magnitude of those fluctuations are small and do not significantly affect the overall shape of the keyhole.

## 2.2. Multi-physics numerical simulations

Our simulations use a multi-physics model to predict the transient evolution of the 3D keyhole shape and the distributions of temperature, pressure, and flow velocity in the substrate, molten pool, keyhole, and the surrounding air. The details of the model are given in Appendix B. Fig. 4 gives an example of typical simulation results, with sub-figure (a) showing the predicted temperature and velocity distributions on the center plane of the track and sub-figure (b) showing the distribution of laser absorption on the 3D keyhole wall.

The three representative cases shown in red (case 1), blue (case 2), and green (case 3) in Fig. 2 were simulated with our multi-physics model. The typical predicted keyhole shapes for the three cases are shown and compared with the DXR observations in Fig. 5. We compare the average keyhole depth (denoted as  $\bar{d}_k$ ), average keyhole width at mid-depth (denoted as  $\bar{w}_k$ ), and average front wall inclination (denoted as  $\bar{\alpha}$ ) from the DXR images and modeling results for the three cases in Table 1, which shows a reasonably good agreement. Here the average

values are calculated based on the measurements of corresponding variables at multiple moments from either DXR or simulation results. Furthermore, the model also successfully captures the dynamic keyhole fluctuation. For example, multiple snapshots from different moments in the simulation of case 1 are shown in Fig. 5 (f)-(h), which closely resemble the different keyhole shapes captured by the DXR in Fig. 5 (a)-(c).

Beyond the capability to predict keyhole shape and fluctuation, the model also predicts the laser absorption by the keyhole, as shown in Fig. 5 (f)-(j). By integrating all the absorbed laser power over the entire keyhole, we find the total laser absorption to be  $\sim 322$  W,  $\sim 292$  W, and  $\sim 186$  W for the three respective cases, as given in Table 1. With the incident laser power as 416 W, the total laser absorptivity of the keyhole is 80%, 70%, and 48% for the three cases, respectively. These values are very close to the in-situ measurement of laser absorption of keyhole in SS316 reported in [19].

## 3. Discussion

In this section, we leverage the modeling results to discuss the physics of keyhole formation and fluctuation. As explained below, the distribution of laser absorption directly affects the temperature, surface evaporation, and fluid flow in the process, all of which affect the geometry of front and rear keyhole wall. The keyhole shape, in turn, alters the distribution of laser absorption.

### 3.1. Laser absorption in dynamic keyhole

To the best of our knowledge, it is still challenging to measure through experimentation the spatial distribution and temporal variation of laser absorption by a moving keyhole. Our

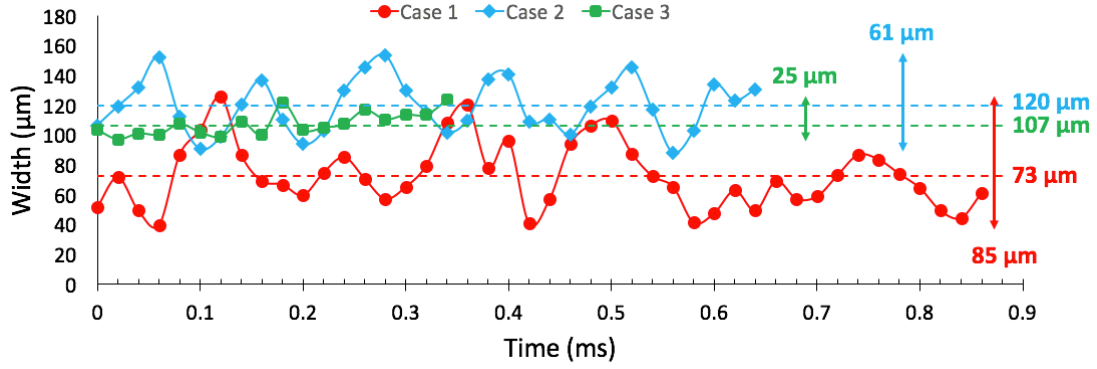


Figure 3: Temporal variation of keyhole width in the three selected cases: Case 1 at  $P = 416$  W,  $V = 300$  mm/s; Case 2 at  $P = 416$  W,  $V = 400$  mm/s; Case 3 at  $P = 416$  W,  $V = 800$  mm/s. The solid dotted lines show the instantaneous width, the dashed lines show the average width, and the double-headed arrows show the magnitudes of width fluctuation.

		Case 1 $P = 416$ W $V = 300$ mm/s	Case 2 $P = 416$ W $V = 400$ mm/s	Case 3 $P = 416$ W $V = 800$ mm/s
Average depth ( $\bar{d}_k, \mu m$ )	<b>DXR</b>	$\sim 370$	$\sim 250$	$\sim 118$
	<b>Model</b>	$\sim 405$	$\sim 257$	$\sim 103$
Average width at mid-depth ( $\bar{w}_k, \mu m$ )	<b>DXR</b>	$\sim 73$	$\sim 120$	$\sim 103$
	<b>Model</b>	$\sim 80$	$\sim 110$	$\sim 140$
Average front wall inclination ( $\bar{\alpha}, degrees$ )	<b>DXR</b>	$\sim 9$	$\sim 12$	$\sim 37$
	<b>Model</b>	$\sim 9$	$\sim 13$	$\sim 26$
Total absorption ( $W$ )	<b>Model</b>	332	292	186
Fresh ray absorption ( $W$ )	<b>Model</b>	136	135	141
Reflected ray absorption ( $W$ )	<b>Model</b>	196	157	45
Reflected ray absorption on front wall ( $W$ )	<b>Model</b>	86	70	0
Reflected ray absorption on rear wall ( $W$ )	<b>Model</b>	110	87	45

Table 1: Keyhole dimensions and laser absorption in the three selected cases. The keyhole dimensions are quantified by the keyhole depth, width at mid-depth, and front wall inclination. The laser absorption is quantified by the total absorption, fresh ray absorption, and reflected ray absorption.

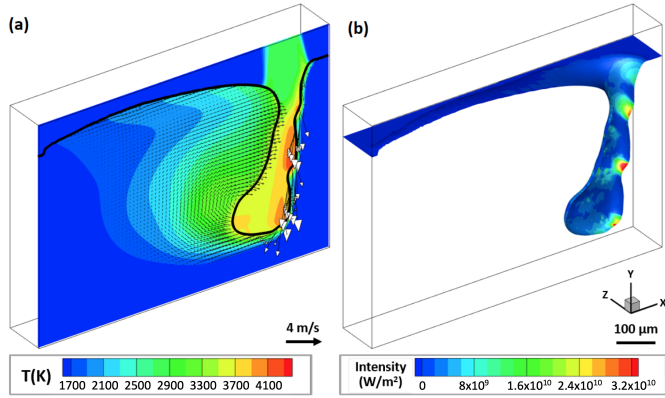


Figure 4: Typical results of 3D simulation of laser-induced keyhole. (a) shows the predicted temperature and velocity on the 2D center plane (velocity in the gas region is hidden for image clarity), and (b) shows the distribution of laser absorption on the 3D keyhole wall.

multi-physics model provides quantitative information regarding this issue.

### 3.1.1. Spatial distribution of laser absorption

Figs. 6(a)-(c) show the spatial distribution of laser absorption of all laser rays. We break down the absorption of all laser light into fresh ray absorption and reflected ray absorption. Here the fresh rays refer to those entering the keyhole directly from the laser source that have not been absorbed by the keyhole wall (as denoted by the solid red lines in Fig. 1). After the fresh rays are partially absorbed by the keyhole wall for the first time, they become reflected rays (as denoted by the dashed red arrows in Fig. 1) and stay inside the keyhole where they experience multiple additional impingements and partial absorption before they escape from the keyhole. The variation in fresh ray absorption intensity and reflected ray absorption are shown in Figs. 6(d)-(f) and (g)-(i), respectively. The powers for fresh ray absorption and reflected ray absorption are given in Table 1.

The fresh ray absorption takes place solely on the front keyhole wall and the absorption power is very similar in the three cases (136 W, 135 W, and 141 W). With the incident power being 416 W, the average absorptivity for the fresh ray on the front keyhole wall is approximately 33%. The spatial distributions of fresh ray absorption are quite different in the three cases. In cases 1 and 2, noticeable protrusions can be found on the front keyhole wall. The fresh ray absorption is concentrated on the up-side of the protrusions and generates very high local absorption intensities ( $>3 \times 10^{10} \text{ W/m}^2$ ). In case 3, the front keyhole wall is flat and the absorption intensity is fairly uniform throughout the front wall ( $\sim 2.5 \times 10^{10} \text{ W/m}^2$ ).

The distribution of reflected ray absorption is dependent on the keyhole shape. In case 1, the keyhole has a larger width at the bottom than near the top, so the reflected rays can get trapped in the keyhole to experience multiple (usually more than four) reflections before they escape. The reflected ray absorption is 196 W, much higher than the fresh ray absorption (136 W). The absorption is spread over the entire keyhole in a non-uniform manner, with a slightly larger fraction on the rear

wall (110 W) than on the front wall (86 W). The reflected rays can generate absorption intensity as high as  $6 \times 10^9 \text{ W/m}^2$  on the keyhole wall. While reflected rays completely determine the keyhole wall temperature on the rear keyhole wall, they just have minor effects on the front wall compared with the high absorption intensities caused by fresh ray absorption on the up-side of the protrusion. In case 2, the absorption of reflected rays is distributed in a similar manner as in case 1. In case 3, the keyhole is wide compared to the spot size on top, which offers a large exit for the rays to escape. The reflected rays can be absorbed by the rear keyhole wall for at most one time before they leave the keyhole. These rays are not reflected back to the front wall, so there is no reflected ray absorption on the front wall, which lowers the total absorptivity. The decreased total absorptivity in the cases of higher scanning speed and lower molten pool depth is consistent with the experimental observation in [19].

### 3.1.2. Temporal variation of laser absorption

As the keyhole shape changes dynamically during the process, the laser absorption constantly deviates by a small amount from the results shown in Fig. 6 and Table 1. Here we select three scalar variables to quantify the spatial distribution at each moment: total laser absorption, fresh ray absorption, and keyhole wall area above critical absorption intensity (denoted as  $S_{critical}$ ). The term  $S_{critical}$  is the total area of the keyhole wall regions where the local absorption is above the critical power intensity for evaporation, which is estimated to be  $1 \times 10^9 \text{ W/m}^2$  [4]. Evaporation is expected to occur in these regions. Fig. 7 (a) shows larger fluctuations of total laser absorption ( $\sim 40 \text{ W}$ ) in case 1 and 2 than in case 3 ( $< 10 \text{ W}$ ). This indicates a less stable keyhole shape in the first two cases, which is consistent with the experimental observation of keyhole fluctuation in Fig. 3. Fig. 7 (b) shows very similar fresh ray absorption (between 130 and 140 W) and only minor fluctuations for all the three cases. This suggests that fresh ray absorption is not highly dependent on the front wall geometry. This also suggests that the fluctuations of the total absorption in case 1 and 2 are because of the randomness in the reflected ray absorption. Fig. 7 (c) shows that the total keyhole wall area of  $\sim 4.5 \times 10^{-8} \text{ m}^2$  in case 1 and  $\sim 3.5 \times 10^{-8} \text{ m}^2$  in case 2 (both with fluctuations of  $>3 \times 10^{-9} \text{ m}^2$ ) have sufficient laser absorption to trigger local evaporation. The regions include the up-side of the protrusions on the front keyhole wall and the scattered locations on the rear keyhole wall. In case 3, the laser absorption of around  $1 \times 10^{-8} \text{ m}^2$  (with a fluctuation of  $< 1 \times 10^{-9} \text{ m}^2$ ) of the keyhole wall can be above the critical intensity. The regions include the entire front keyhole wall and scattered regions on the rear wall.

In the following two subsections, we discuss the effects of laser absorption on the shape and fluctuation of both the front and rear keyhole wall.

## 3.2. Dynamics of the front keyhole wall

The front keyhole wall is primarily controlled by the fresh ray absorption. The power absorbed of fresh rays is very similar for the three cases but the front keyhole shape and spatial

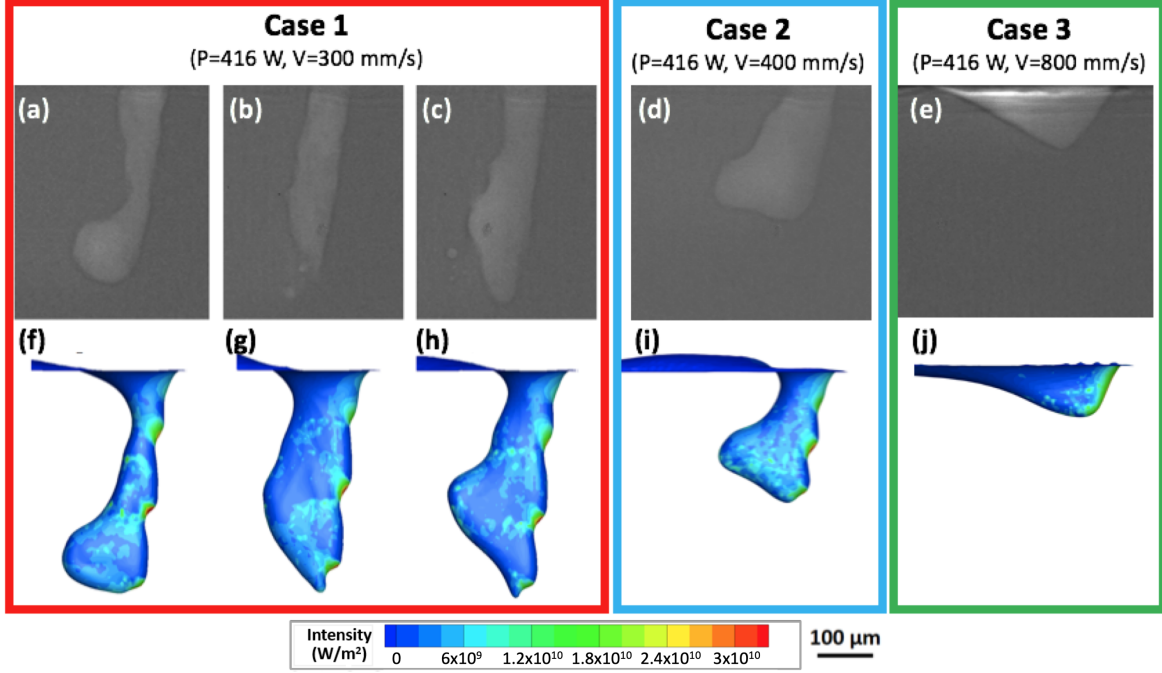


Figure 5: Comparison of keyhole shapes from DXR observation and simulation results for the three selected cases. (a)-(e): DXR images of keyhole shape. (f)-(j): Simulated keyhole shape and distribution of laser absorption. For illustrative purposes, different instances are shown for case 1 which exhibits the most fluctuation out of the three cases. (a)-(c) case 1 at times  $t_0$ ,  $t_0 + 140ms$ , and  $t_0 + 340ms$ . (f)-(h) are the predictions at three selected instances from the simulation.

distribution of fresh ray absorption intensity are quite different in the three cases. In cases 1 and 2, the front keyhole wall is less inclined with noticeable protrusions on the wall. The fresh ray absorption is concentrated on the up-side of the protrusions and locally generates very high absorption intensity ( $>3 \times 10^{10} W/m^2$ ). In case 3, the front keyhole wall is more inclined and smooth, and the absorption intensity is fairly uniform ( $2.5 \times 10^{10} W/m^2$ ). The spatial distribution of fresh ray absorption decisively affects the geometry of the front keyhole wall, including the front wall inclination and the protrusion generation on the front wall. The front wall geometry, in turn, alters the distribution of fresh ray absorption.

### 3.2.1. Inclination of front keyhole wall

A series of analytical models have already been proposed to estimate the front wall inclination and keyhole depth based on processing parameters and thermo-physical properties of the materials [6, 5, 43, 44]. Inspired by these works, here we present a similar analysis based on our numerical simulation results, which include more information regarding the dynamic thermofluidic phenomena during the laser-induced keyholing process.

The front wall inclination is determined by the combination of the laser scanning speed  $V_l$  and the drilling velocity  $V_d$ , as estimated by Eqn. 1:

$$\bar{\alpha} = \text{atan}\left(\frac{V_l}{V_d}\right). \quad (1)$$

Here,  $V_l$  is 300 mm/s, 400 mm/s and 800 mm/s for the three cases, and  $V_d$  can be considered to be the vertical component of

the liquid flow velocity on the front keyhole wall. The average  $V_d$  is found from the simulations to be 6.5 m/s, 3.4 m/s, and 2.2 m/s for the three cases. If we plug the  $V_l$  and  $V_d$  values into Eqn. 1, the average inclination angles of the three cases are found to be  $3^\circ$ ,  $7^\circ$ , and  $20^\circ$ , reasonably close to the measurement results from the DXR observations and simulations, as already given in Table 1.

Note that approximately the same amount of power ( $\sim 130$  W) is deposited on the front keyhole wall due to the fresh ray absorption in the three cases, but the resultant  $V_d$  is different. The term  $V_d$  can be estimated as

$$V_d = \int_{t_{dwell}} a_d dt. \quad (2)$$

Here  $a_d$  is the acceleration for drilling primarily due to the recoil pressure. According to the simulations, the average acceleration due to the recoil pressure is approximately  $2.8 \times 10^4 m/s^2$ ,  $2.7 \times 10^4 m/s^2$ , and  $2.3 \times 10^4 m/s^2$  for the three cases. The term  $t_{dwell}$  is the dwell time of fresh rays illuminating the front keyhole wall, which is calculated according to Eqn. 3:

$$t_{dwell} = \frac{d_l}{V_l}. \quad (3)$$

Here,  $d_l$  is the diameter of the laser spot, which is  $100 \mu m$  for our work, and  $V_l$  is the laser scanning speed. The fresh ray dwell time is found to be  $3.33 \times 10^{-4} s$ ,  $2.50 \times 10^{-4} s$ , and  $1.25 \times 10^{-4} s$  for the three cases.

In case 1, multiple protrusions on the front wall lead to fresh ray absorption localization on the regions of very small surface

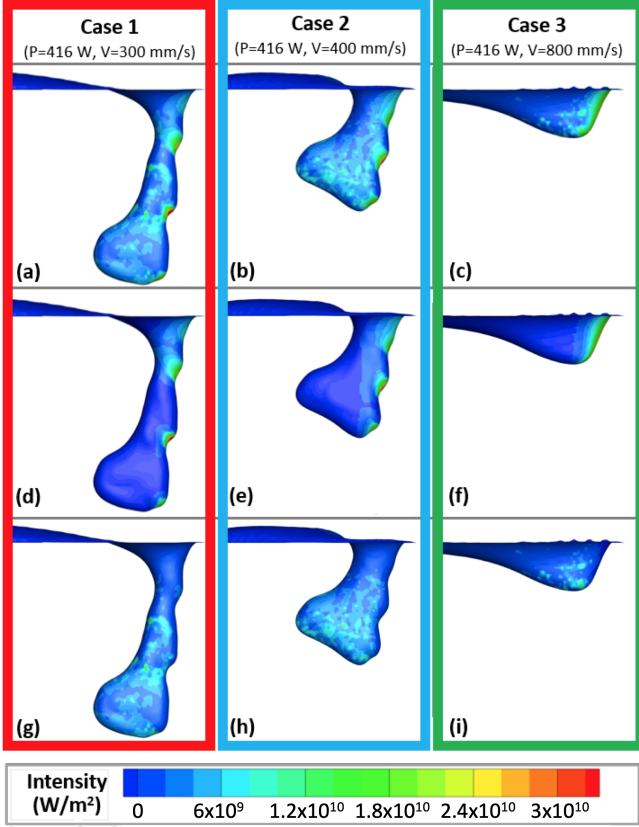


Figure 6: Distribution of laser absorption intensity: (a)-(c) for all rays, (d)-(f) for fresh rays, and (g)-(i) for reflected rays in the three selected cases.

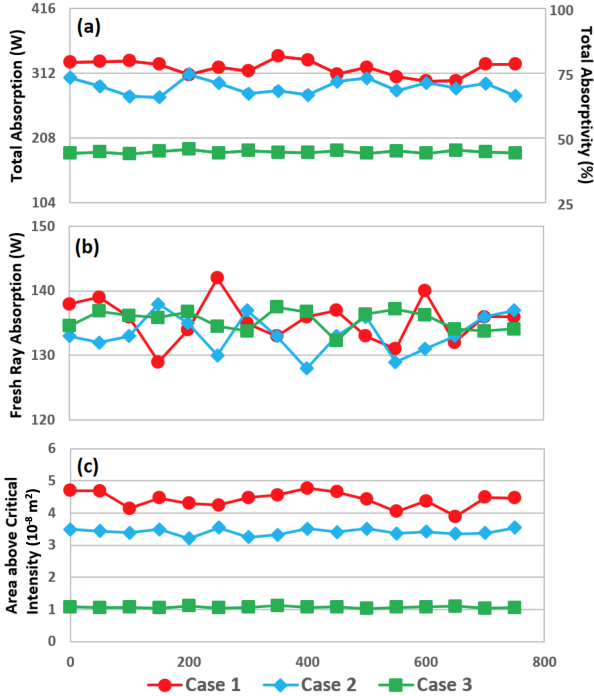


Figure 7: Temporal variations of (a) total laser absorption and corresponding absorptivity (with respect to the input laser power 416 W), (b) fresh ray absorption, and (c) keyhole wall area with absorption intensity above critical value. For all three cases the experiments were performed at the same laser power  $P = 416$  W and varying scanning speeds: Case 1 at  $V = 300$  mm/s; Case 2 at  $V = 400$  mm/s; Case 3 at  $V = 800$  mm/s.

area on the up-side of those protrusions, and the resulting absorption intensity is rather high ( $3.2 \times 10^{10} \text{ W/m}^2$ ). The local temperature becomes very high (around 4200 K) and induces intense evaporation. A strong recoil pressure (as high as  $1 \times 10^6$  Pa) is available to generate the highest acceleration for drilling (i.e.,  $a_d$ ). Meanwhile, the time for acceleration is the longest (i.e.,  $t_{dwell} = 3.33 \times 10^{-4}$  s). The drilling velocity on the front wall is therefore the highest (6.5 m/s).

In case 2, protrusions are also present on the front keyhole wall. In this case the absorption intensity ( $3.1 \times 10^{10} \text{ W/m}^2$ ), surface temperature (4200 K), and recoil pressure ( $1 \times 10^6$  Pa) on the front wall are similar to those in case 1. However, a shorter fresh ray dwell time ( $2.50 \times 10^{-4}$  s) is available to accelerate the drilling velocity, leading to a decrease in  $V_d$  (3.4 m/s).

In case 3, the front wall is rather flat and the fresh ray absorption is uniformly distributed over the entire front wall, leading to a relatively low absorption intensity ( $2.5 \times 10^{10} \text{ W/m}^2$ ) and hence the surface temperature is relatively low (around 4000 K). A lower recoil pressure ( $6 \times 10^5$  Pa) is available for an even shorter fresh ray dwell time ( $1.25 \times 10^{-4}$  s) to accelerate the drilling velocity. Moreover, since the front keyhole wall is flat, the pressure gradient due to the recoil pressure is along the normal direction of the front wall. Not the entire pressure gradient, but only its vertical component, is used to accelerate the drilling velocity. As a result, the drilling velocity is the lowest (2.2 m/s) in case 3.

### 3.2.2. Protrusion dynamics on the front keyhole wall

Protrusions have been found on the front keyhole wall in cases 1 and 2, and they facilitate the localization of fresh ray absorption to induce high absorption intensity and strong evaporation. The simulations well demonstrate the generation and movement of these protrusions.

For any segment on the front keyhole wall, e.g., the blue segment in Fig. 8 (a), if the local inclination angle is  $\alpha$ , the incident angle  $\beta$  of the incident fresh ray on this segment can be calculated as  $\beta = 90^\circ - \alpha$ . The absorption intensity due to the fresh ray can be calculated as

$$\begin{aligned}
 I_{abs, fresh} &= \frac{I_{fresh} A(\beta) \Delta S_{ray}}{\Delta S_{seg}} \\
 &= I_{fresh} A(\beta) \cos \beta \\
 &= I_{fresh} R_{intensity}.
 \end{aligned} \tag{4}$$

Here,  $I_{abs, fresh}$  is the absorption intensity on this segment due to the incident fresh ray, the power intensity of which is  $I_{fresh}$ . The term  $A(\beta)$  is the local laser absorptivity as a function of the incident angle  $\beta$ . The dependence is shown graphically by the purple curve in Fig. 8 (b), which is calculated with the Fresnel equation. The term  $\Delta S_{ray}$  is the cross-section area of the ray. The term  $\Delta S_{seg}$  is the surface area of the segment, which can be calculated as  $\Delta S_{ray} = \Delta S_{seg} \cos \beta$ . The multiplication term  $A(\beta) \cos \beta$  calculates the ratio of absorption intensity over incident laser intensity. This intensity ratio,  $R_{intensity}$ , as a function of  $\beta$  is shown by the orange curve in Fig. 8 (b).

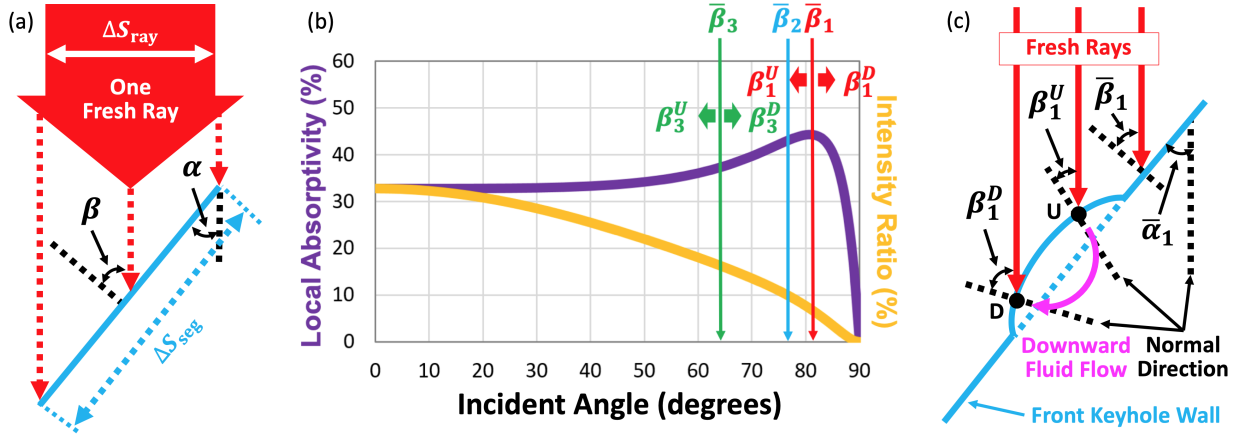


Figure 8: Laser absorption on the keyhole wall. (a) The absorption of one fresh laser ray by a linear segment of the front keyhole wall. (b) Laser absorption by keyhole wall: The purple curve shows the local absorptivity as a function of incident angle. The orange curve shows the ratio of the absorbed laser power intensity on the front keyhole wall over the incident laser power intensity from the fresh laser ray. The red ( $\beta_1^U, \beta_1^D, \beta_1^P$ ), blue ( $\beta_2$ ), and green ( $\beta_3^U, \beta_3^D, \beta_3^P$ ) terms mark out the incident angles of the fresh ray on the front keyhole wall for cases 1, 2, and 3, respectively, and will be used in the discussion, subsection 3.2. (c) Non-uniform absorption of fresh rays across a protrusion on front keyhole wall. Note that the inclination angle and protrusion size are exaggerated in this figure for clarity of illustration.

In case 1, the protrusions usually start near the top of the front keyhole wall on the convex surface because of the natural transition from the horizontal top surface ahead of the keyhole to the inclined front keyhole wall (see protrusion A in Fig. 9) and these protrusions flow down along the front keyhole wall until they reach the keyhole bottom (see protrusion B and C in Fig. 9). The distribution of fresh ray absorption intensity on these protrusions is not uniform, as illustrated in Fig. 8 (c). The average front keyhole wall inclination is  $\bar{\alpha}_1 = 9^\circ$ , and correspondingly the average incident angle of the fresh laser rays on the front wall is  $\bar{\beta}_1 = 90^\circ - \bar{\alpha}_1 = 81^\circ$ . For any point on the up-side of the protrusion (e.g., point U), we can draw the local incident angle of a fresh ray on point U (i.e.,  $\beta_1^U$  in Fig. 8 (c)) and find  $\beta_1^U < \bar{\beta}_1$ . Similarly, if we can find one point from the down-side of the protrusion (e.g., point D) and draw the incident angle of a fresh ray on this point (i.e.,  $\beta_1^D$  in Fig. 8 (c)), we should find  $\beta_1^D > \bar{\beta}_1$ . By mapping the values of  $\bar{\beta}_1$ ,  $\beta_1^U$ , and  $\beta_1^D$  in Fig. 8 (b), it is evident that the intensity ratio on the up-side of the protrusion ( $R_{intensity}^U$ ) is generally higher than that on the down-side of the protrusion ( $R_{intensity}^D$ ), i.e.,  $R_{intensity}^U > R_{intensity}^D$ . With similar power intensity  $I_{fresh}$  for the fresh rays incident upon points U and D, Eqn 4 gives  $I_{abs, fresh}^U > I_{abs, fresh}^D$ , i.e., the fresh ray absorption intensity is higher on the up-side than on the down-side of the protrusion. As shown in Fig. 6(d), the absorbed intensity is  $> 3 \times 10^{10} \text{ W/m}^2$  on the up-side of the protrusions, and is  $< 2 \times 10^9 \text{ W/m}^2$  on the down-side of the protrusions. In certain scenarios, a portion of the down-side area can even be completely shaded by the protrusion and receive zero illumination by fresh rays. Thanks to the non-uniform distribution of fresh ray absorption, the temperature is considerably higher on the up-side than the down-side on the protrusion. Fig. 5(d) shows the temperature on the up-side of the protrusion at around 4200 K, which is well above the boiling point of the metal (3375 K) and causes strong evaporation and recoil pressure ( $1 \times 10^6 \text{ Pa}$ ). On the other hand, the temperature on the down-side is around

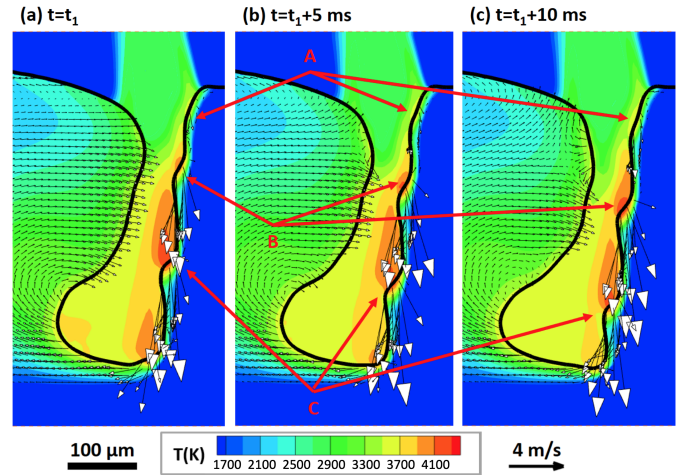


Figure 9: Three consecutive instants in time showing the generation and downward motion of protrusions on front keyhole wall in case 1. Protrusion A starts to form on the convex surface in the transition zone between the horizontal top surface and inclined front keyhole wall. Protrusion B and C are moving downwards along the front keyhole wall (notice the high velocity of the fluid flow on the front keyhole wall).

2900 K; hence, no evaporation and recoil pressure will be induced. A remarkable pressure difference is created between the two sides of the protrusion, which induces a downward liquid flow, as indicated by the pink arrow in Fig. 8 (c). This downward flow causes the protrusions to flow downwards along the front keyhole wall as the protrusions grow in size. The intermittent generation of protrusion at the top of the front keyhole wall and their downward motion means that the front wall appears to be wavy, which is consistent with the DXR observation for case 1.

In case 2, the average front keyhole wall inclination is  $\bar{\alpha}_2 = 13^\circ$ , and correspondingly the average incident angle of the fresh laser rays on the front wall is  $\bar{\beta}_2 = 77^\circ$ . Protrusions are also

found in the DXR observations and in the numerical simulations for this case for reasons identical to those described earlier in case 1. In case 3, the front keyhole wall becomes very flat and no protrusions are observed in the DXR measurements and the simulation. This suggests that the front wall becomes more resistant to protrusion generation compared to cases 1 and 2. The average front keyhole wall inclination for case 3 is  $\bar{\alpha}_3 = 26^\circ$ , and correspondingly the average incident angle of the fresh laser rays on the front wall is  $\bar{\beta}_3 = 64^\circ$ . Given a random protrusion on the front wall (similar to the one in Fig. 8 (c)), the incident angle of fresh rays on the up-side and down-side of the protrusion (denoted as  $\beta_3^U$  and  $\beta_3^D$ ) are slightly different than  $\bar{\beta}_3$ . As marked out in Fig. 8 (b), the intensity ratio for both  $\beta_3^U$  and  $\beta_3^D$  are reasonably high, indicating that both the up-side and down-side of the protrusion receive sufficient intensity to induce evaporation and recoil pressure. In this case, the liquid metal is driven away from both the up-side and down-side of the protrusion, and the protrusion is suppressed so that the front wall remains flat. The driven liquid will flow around the side of the keyhole and enters the molten pool trailing the keyhole, as will be described in details in the next subsection .

### 3.3. Dynamics of the rear keyhole wall

The rear keyhole wall is found to have quite different shapes in the three cases. The keyhole width in the upper part of the keyhole is relatively small in case 1 and 2 but fairly large in case 3. The general shape of the rear keyhole wall is found to be independent of the laser absorption on the rear wall. Instead, it is closely related to the fluid dynamics initiated on the front keyhole wall. Furthermore, the general shape of the rear wall significantly alters the distribution of reflected ray absorption, which strongly affects the fluctuation of rear wall from its average position.

#### 3.3.1. Molten pool fluid dynamics and rear keyhole wall shape

The predicted flow patterns in the molten pool trailing the keyhole are shown in Fig. 10. The pattern is most obvious in case 1. Two vortices are evident on the center plane, indicated by “A” and “B” in Fig. 10(a). Vortex “A” is located in the upper part of the molten pool with a counter-clockwise flow, which is primarily driven by the thermocapillary force on the top surface of the molten pool. Vortex “B” is located in the lower part of the molten pool with a clockwise flow direction. This vortex is initiated on the front keyhole wall. Driven by the recoil pressure, the molten metal flows around the keyhole from the left or right sides and the bottom of the keyhole and enters the trailing molten pool. This flow moves towards the tail of the molten pool bottom and gradually turns upward along the fusion line. The upward flow collides with the downward flow in the upper vortex, and these two flows both turn to flow towards the rear keyhole wall. In a horizontal plane in the upper part of the molten pool close to the top surface, one vortex can be found in one half of the molten pool, as marked out by “C” in Fig. 10(d). The flow starts on the front keyhole wall and goes around the keyhole from the side, moves backwards towards the molten pool tail, and reverse the flow direction to be towards the rear

keyhole wall. The flow patterns in cases 2 and 3 are essentially similar to the one in case 1, except that vortex “B” becomes very small because the molten pool is shallow.

Note that the metal flows in all the above three vortices, either on the center plane, i.e. vortices “A” and “B” in Fig. 10(a)-(c), or the horizontal plane i.e. vortex “C” in Fig. 10(d)-(f), start with a motion towards the molten pool tail, decelerate, and turn around to flow towards the rear keyhole wall. The liquid pressure near the rear keyhole wall is relatively low (primarily because of the local convex surface and hence the negative surface tension of the rear keyhole wall), so there is usually a pressure gradient towards the rear keyhole wall. The metal flows are accelerated by this pressure gradient as they flow towards the rear keyhole wall. When the metal arrives at the rear keyhole wall, the horizontal component of the flow speed is accelerated to equal  $V_l$ . This ensures that the rear keyhole wall can catch up with the front keyhole wall so that the distance between front and rear keyhole walls (i.e., the keyhole width) remains relatively constant (with some fluctuation around the average width).

In case 1, as protrusions are generated on the front keyhole wall, the recoil pressure primarily drives the molten metal to flow downwards so that its downward component (i.e., the drilling velocity,  $V_d = 6.5$  m/s) dominates the resultant flow, as shown in Fig. 10(a). In a horizontal plane in the upper part of the molten pool, close to its top surface, as shown in Fig. 10(d), the backward component of the flow velocity  $V_b$ , is correspondingly very small ( $V_b = 300$  mm/s). This slow backward flow is soon reversed and accelerated to  $V_l = 300$  mm/s towards the rear keyhole wall. Since  $V_b$  and  $V_l$  are both small compared to the scan speed, the velocity reversion process can be completed in a very short time and travel distance so that the rear keyhole wall is very close to the front keyhole wall, i.e., the keyhole width is very small in the upper part of the keyhole. In case 2, the flow velocity in the horizontal plane as shown in Fig. 10(e) is similar to that in case 1 and hence the keyhole width is also small in the upper part of the keyhole.

In case 3, however, the front keyhole is more inclined and flatter, and the recoil pressure is more uniformly distributed on the front keyhole wall, which pushes the molten metal around the keyhole from the sides. As shown in Fig. 10(f), the backward flow becomes very fast ( $V_b = 700$  mm/s), and it takes a relatively long time and travel distance for the flow to reverse its direction and accelerate to the high laser scanning speed of  $V_l = 800$  mm/s in this case. By the time the flow reaches the rear keyhole wall, the front keyhole wall has traveled forward for quite a long distance, and hence the distance between the front and rear keyhole wall, i.e., the keyhole width, becomes rather large in the upper part of the keyhole.

With the keyhole width in cases 1 and 2 being small near the top surface, the “trapping” effect encourages higher absorption for reflected rays (196 W for case 1 and 157 W for case 2). The reflected rays significantly heat the rear keyhole wall (primarily in the lower portion) to above the boiling point. Local evaporation and recoil pressure is induced, pushing the rear keyhole wall backwards and enhancing the keyhole width. With the keyhole wall area much larger in case 1 ( $\sim 7 \times 10^{-8} \text{ m}^2$ ) than in case 2 ( $\sim 4.5 \times 10^{-8} \text{ m}^2$ ), the reflected

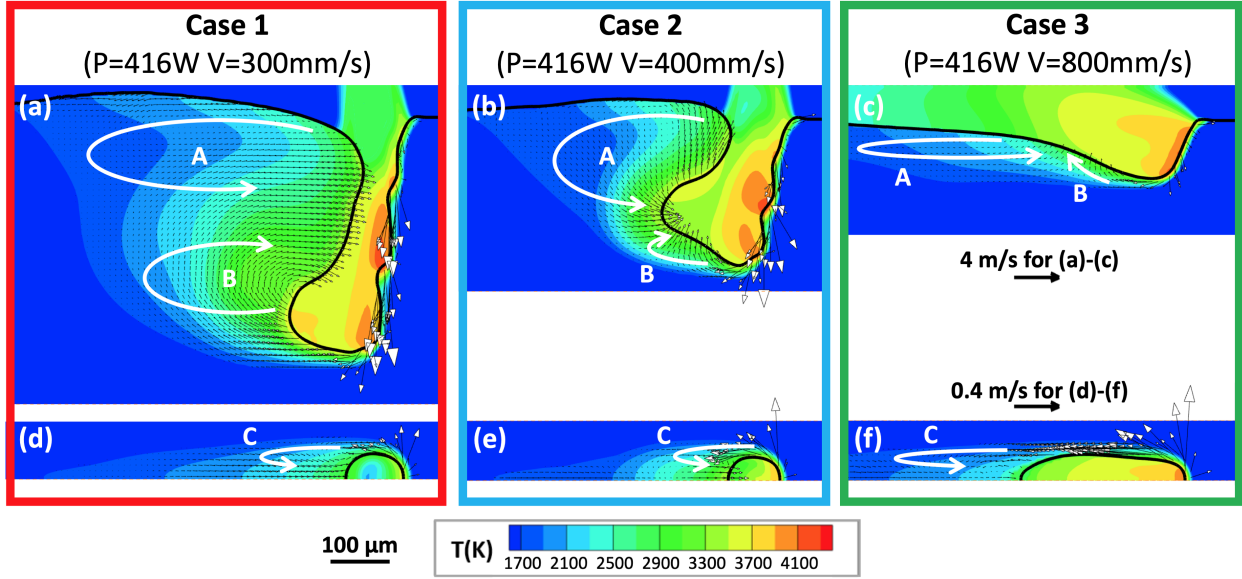


Figure 10: Simulation results of the temperature and velocity fields in the three selected cases. (a)-(c) show the temperature and velocity fields on the center plane from the simulations. (d)-(f) show the horizontal plane looking from the top of the keyhole near the surface of the substrate from the simulations. Note that the velocity field for vapor is not shown. The vortices labeled “A”, “B” & “C” are discussed in subsection 3.3.1.

ray absorption intensity density should be generally lower in case 1 (averaged at  $\sim 2.8 \times 10^9 \text{ W/m}^2$ ) than in case 2 (averaged at  $\sim 3.5 \times 10^9 \text{ W/m}^2$ ). As a result, the temperature on the rear keyhole wall in case 1 averages  $\sim 3300 \text{ K}$  with the maximum value above  $3600 \text{ K}$ , while in case 2 the average temperature is above  $3400 \text{ K}$  with the maximum value above  $3700 \text{ K}$ . Due to the slightly higher temperature in case 2, a higher recoil pressure is available on the rear wall to push it further away from the front wall. Therefore, the keyhole width is larger in case 2 ( $120 \mu\text{m}$ ) than in case 1 ( $73 \mu\text{m}$ ), as given in Fig. 3.

In case 3, the keyhole width is rather large near the surface of the keyhole, which offers a large exit for the rays to escape. According to our simulation, all the reflected rays will only be absorbed once by the rear keyhole wall, and their reflections will be able to leave the keyhole. Therefore, the reflected ray absorption power is drastically reduced to  $56 \text{ W}$  and it causes no evaporation on the rear keyhole wall to modify the general shape of the keyhole.

### 3.3.2. Dynamic fluctuation of rear keyhole wall

Strong keyhole fluctuation is found in cases 1 and 2, and it is primarily caused by the random movement of the rear keyhole wall away from its general shape. Such random movement of the rear keyhole wall results from the randomly varying distribution of reflected rays absorbed on the rear keyhole wall, which is initiated by the wavy front from the protrusions on the front keyhole wall. While the fresh rays are presumably parallel to each other before they land on the protrusions, the reflected rays follow different directions and illuminate the rear keyhole wall at different locations. The directions of the reflected rays become essentially random beyond the first reflection. Therefore, no fixed pattern of absorption intensity distribution can be found for reflected rays, and hot spots with high absorption

intensities can appear at random locations. At each hot spot, local evaporation is induced and recoil pressure is generated that pushes the rear keyhole wall backwards, creating a local dent on the rear keyhole wall. As the hot spots wander, the dents move accordingly. There is a hot spot near the bottom in Fig. 5(f) and also around the middle depth in Fig. 5(h).

The fluctuation is significantly reduced in case 3 for two reasons. First, the front keyhole wall is nearly flat with a relatively uniform distribution of laser absorption and recoil pressure. This helps the molten metal on the front keyhole wall to develop a steady flow going around the keyhole to build a stable rear keyhole wall. Second, the reflected ray absorption is insignificant on the rear keyhole wall. No evaporation is induced and thus no meaningful disturbances on the rear keyhole wall.

### 3.4. Effect of major forces on the keyhole dynamics

After the discussion of the laser absorption and the dynamic phenomena on the front and rear keyhole wall, here we present a direct comparison of various driving forces for both the molten pool flow and keyhole evolution. The major driving forces to be investigated are the recoil pressure, capillary force, and thermocapillary force. The orders of magnitude of these forces at different locations of the keyhole were calculated from the simulation results (formula given in Appendix B) and are listed in Table 2. Note that the recoil pressure and capillary force are applied along the normal direction of the molten pool surface and keyhole wall, while the thermocapillary force is applied along the tangential direction.

On the front keyhole wall, the temperature is above  $4000 \text{ K}$  because of the intensive heating from the fresh laser rays, which induces strong evaporation to generate a strong recoil pressure on the order of  $10^5$  to  $10^6 \text{ Pa}$ . This pressure is applied along the

	Case 1 $P = 416 \text{ W}$ $V = 300 \text{ mm/s}$	Case 2 $P = 416 \text{ W}$ $V = 400 \text{ mm/s}$	Case 3 $P = 416 \text{ W}$ $V = 800 \text{ mm/s}$
<b>Front Keyhole Wall</b>			
Maximum Temperature (K)	$\sim 4200$	$\sim 4200$	$\sim 4000$
Maximum Recoil Pressure (Pa)	$10^6$	$10^6$	$10^5$
Maximum Curvature (1/m)	$-10^4$	$-10^4$	$-10^4$
Maximum Capillary Force (Pa)	$-10^4$	$-10^4$	$-10^4$
Maximum Temperature Gradient (K/s)	$10^7$	$10^7$	$10^7$
Maximum Thermocapillary Force (Pa)	$10^4$	$10^4$	$10^4$
<b>Rear Keyhole Wall</b>			
Maximum Temperature (K)	$\sim 3600$	$\sim 3700$	$\sim 2800$
Maximum Recoil Pressure (Pa)	$10^5$	$10^5$	0
Maximum Curvature (1/m)	$-10^4$	$-10^4$	$-10^4$
Maximum Capillary Force (Pa)	$-10^4$	$-10^4$	$-10^4$
Maximum Temperature Gradient (K/s)	$10^6$	$10^6$	$10^6$
Maximum Thermocapillary Force (Pa)	$10^3$	$10^3$	$10^3$
<b>Top Surface of Molten Pool</b>			
Maximum Temperature (K)	$< 3000$	$< 3000$	$< 3000$
Maximum Recoil Pressure (Pa)	0	0	0
Maximum Curvature (1/m)	$10^3$	$10^3$	$-10^3$
Maximum Capillary Force (Pa)	$10^3$	$10^3$	$-10^3$
Maximum Temperature Gradient (K/s)	$10^6$	$10^6$	$10^6$
Maximum Thermocapillary Force (Pa)	$10^3$	$10^3$	$10^3$

Table 2: Order of magnitude of the major forces driving the molten pool flow and keyhole evolution. These forces are evaluated at the front keyhole wall, rear keyhole wall, and top surface of the molten pool in the three selected cases studied in this paper.

normal direction of the keyhole wall towards the liquid region and acts as the major force to maintain the inclined front keyhole wall while pushing it forward. Since the front keyhole wall is a concave interface, the curvature ( $K$  in Eqn. B.8) is negative on the order of  $-10^4 \text{ m}^{-1}$ . With the surface tension coefficient ( $\gamma$  in Eqn. B.8) being 1.6 for the liquid metal, the capillary force is on the order of  $-10^4 \text{ Pa}$ . While this force acts along the opposite direction with respect to the recoil pressure, it is at least two orders of magnitude smaller and therefore is overruled by the recoil pressure. With the maximum surface temperature gradient ( $\nabla_s T$  in Eqn. B.3) on the order of  $10^7 \text{ K/m}$  and the surface tension coefficient ( $\partial\gamma/\partial T$  in Eqn. B.3) being 0.0043 for the liquid metal, the thermocapillary force is on the order of  $10^4 \text{ Pa}$ . Although this force is also two orders of magnitude smaller than the recoil pressure, it acts along a different direction from that of the recoil pressure and hence is not totally overruled. It can still effectively drive the liquid metal on the interface to flow from hot regions to cold regions (i.e., the Marangoni flow).

On the rear keyhole wall, the temperature is still above the boiling point in cases 1 and 2. The recoil pressure is on the order of  $10^5 \text{ Pa}$  and is still dominant over the capillary force, which is on the order of  $-10^4 \text{ Pa}$ . However, the temperature of the rear keyhole wall drops below the boiling point in case 3, where no evaporation or recoil pressure are available. The capillary force becomes dominant along the normal direction of the rear keyhole wall. Along the tangential direction, the thermocapillary force is on the order of  $10^3 \text{ Pa}$  in all three cases and still effectively drives a Marangoni flow on the rear keyhole wall.

On the top surface of the molten pool, the temperature is usually below the boiling point, and hence no recoil pressure is available. This area is primarily controlled by the capillary force and thermocapillary force, both of which are on the order

of magnitude of  $10^3 \text{ Pa}$ . The capillary force tends to suppress any unevenness on the top surface. The thermocapillary force drives the Marangoni flow towards the tail and the side of the molten pool, and is primarily responsible for the development of vortex ‘‘A’’ in Fig. 10(a)-(c).

#### 4. Conclusions

In this paper, we present a combination of an advanced multi-physics numerical model with a state-of-the-art dynamic X-ray radiography (DXR) experiments to understand the dynamic phenomena of laser-induced keyholing in stainless steel 304. On the experimental side, in-situ DXR experiments provided observations of the keyhole shape and fluctuation as a function of laser power and scanning speed. As the laser scanning speed is increased at a constant power, the keyhole depth decreases, the front wall inclination and keyhole width increase, and the magnitude of keyhole fluctuation decreases. On the modeling side, our multi-physics model successfully reproduces the typical shapes observed by DXR under different conditions. Moreover, the models provide information regarding the distribution of laser absorption on the keyhole walls and its effects on evaporation, thermofluidic flow, and keyhole shape and fluctuation, all of which are inaccessible via experiment.

On the front keyhole wall, the phenomena are dominated by the absorption of fresh rays. In the case of a lower scanning speed, a higher recoil pressure and a longer fresh ray dwell time are available to accelerate drilling on the front wall, leading to a higher drilling velocity and a smaller inclination angle of the front wall. The incident angle of fresh rays on the front wall is closer to  $90^\circ$ , and the fresh ray absorption becomes less stable. Protrusions form on the top of the front wall and flow downwards, causing unstable wavy fluctuation of the front wall.

At higher scanning speeds, the front wall is more inclined and the fresh ray absorption becomes more stable, generating a flat and stable front wall.

On the rear keyhole wall, the general shape is primarily determined by the fluid dynamics initiated on the front keyhole wall, and the reflected ray absorption is mainly responsible for the fluctuation of the rear wall from its nominal shape. At lower scanning speeds, the melt flow initiated on the front keyhole wall circulates around the keyhole with a lower speed along the horizontal direction. This slow horizontal flow immediately fills the empty space behind the keyhole, resulting in a smaller keyhole width. The smaller keyhole width significantly enhances multiple reflection of the laser light, resulting in higher absorbed power from reflected ray absorption. The distribution of the reflected ray absorption varies significantly over the rear keyhole wall (especially in the lower portion) and causes the rear keyhole wall to fluctuate. At higher scanning speeds, the melt flow goes around the keyhole at a much higher speed along the horizontal direction. The fast horizontal flow does not immediately fill the empty space behind the keyhole, resulting in a larger keyhole width. The reflected ray absorption is considerably lower and does not cause any noticeable fluctuation of the rear keyhole wall.

Multiple driving forces (namely recoil pressure, capillary force, and thermocapillary force) exist on the molten pool surface and keyhole wall, and they are of different significance to the molten pool flow and keyhole behavior. Along the normal direction of the interface, the recoil pressure pushes the molten metal away thus maintaining the opening of the keyhole, while the capillary force tends to suppress any unevenness of the interface. The recoil pressure from evaporation (when present) is usually orders of magnitude larger than the capillary force on both the front and rear keyhole wall, and the capillary force is only significant when the surface temperature is below the boiling point. The thermocapillary force is active along the tangent direction of the interface and drives Marangoni flow. The thermocapillary force is also orders of magnitude smaller than the recoil pressure but its effect is always present.

The combination of DXR observation and multi-physics modeling provides a valuable framework for understanding the complex phenomena in laser-induced keyholes. The framework is expected to contribute to understanding the mechanisms of pore/spatter formation in laser-based additive manufacturing and welding processes.

## Acknowledgments

N.K. and A.D.S. acknowledge the financial support from the Department of Defense Office of Economic Adjustment under award no. ST1605-19-03. X.L. and W.T. thank the financial support from the National Science Foundation under grant CMMI-1752218 and the technical support from the Center for High-Performance Computing at the University of Utah. R.C. and A.D.R. thank the Northrop Grumman Corporation for support of this research. C.Z., N.P. and T.S. are grateful for the Laboratory Directed Research and Development (LDRD) funding from Argonne National Laboratory, provided by the Direc-

tor, Office of Science, of the U.S. Department of Energy under Contract No. DE-AC02-06CH11357. This research used resources of the Advanced Photon Source, a U.S. Department of Energy (DOE) Office of Science User Facility operated for the DOE Office of Science by Argonne National Laboratory under Contract No. DE-AC02-06CH11357.

## Appendix A. Methodology for in-situ observation of laser-induced keyhole with dynamic X-ray radiography

High-speed dynamic X-Ray radiography (DXR) experiments were performed at the 32-ID-B beamline at the APS. Fig. A.11 shows a schematic of the experimental setup. In each case, a SS304 substrate about  $400\ \mu\text{m}$  thick was processed with a specific combination of laser power and scanning speed. The metal specimen was placed inside a SS chamber filled with Argon gas to create an inert environment. The experiments were conducted at room temperature without preheating of the metal specimens. A laser beam of  $\sim 100\ \mu\text{m}$  diameter, shown in Fig. A.11, was used to scan along the centerline of the metal plate, orthogonal to the X-ray beam. The high-speed imaging camera captures a side view of the laser keyhole shape that is exposed on the X-ray detectors and records full field X-ray images with a rate of 50 kHz and a spatial resolution of about  $2\ \mu\text{m}$  per pixel.

Experiments were performed in the parameter window of interest to metal AM. The laser-power  $P$  was varied between 208 and 520W with increments of 104 W, and the laser scanning speed  $V$  between 300 and 1200 mm/s with increments of 100 or 200 mm/s. For the purpose of this study, 14 combinations of  $P$  and  $V$  were tested using the DXR experiment to explore typical cases of the keyhole formation.

## Appendix B. Formulation of the multi-physics modeling of laser-induced keyhole

A multi-physics model is employed to account for keyhole wall movement, laser-matter interaction, and multi-phase and

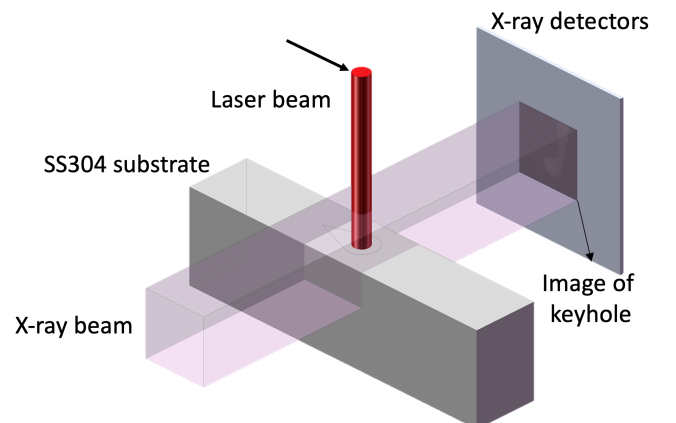


Figure A.11: Sketch of dynamic X-ray radiography experiments. The laser scanning direction is shown by the black arrow.

multi-species thermofluidic flow in the laser-induced keyhole and molten pool. Model inputs include the laser parameters (laser power, spot size, power distribution, scanning speed), substrate geometry, and material properties. The model then predicts the 3D keyhole shape and the 3D distributions of temperature, pressure, and velocity in solid, liquid, and gas phases. The primary formulations of the model are briefly described in what follows, with a more detailed description of the model provided in Refs. [32, 33].

In the current model, the level-set (LS) method [45] is used to track the interface between the condensed phases (solid and liquid metal) and non-condensed phases (ambient gas and metallic vapor). The LS equation is written as:

$$\frac{\partial \varphi}{\partial t} + (\vec{V}_c - \frac{m_{evap}}{\rho_c} \cdot \vec{N}) \cdot \nabla \varphi = 0. \quad (\text{B.1})$$

In Eqn. B.1,  $\varphi$  is the LS function, which quantifies the distance from the centroid of a control volume to the molten pool surface. The molten pool surface (with a portion of it being the keyhole wall) is captured by the zero iso-LS surface, and the LS function is defined to be negative in the condensed phases and positive in the non-condensed phases. The two terms in the bracket of the left-hand-side (LHS) of Eqn. B.1 are two components that drive the interface motion. The first term,  $\vec{V}_c$ , is the convection velocity of the condensed phase at the interface. The second term is the surface recession velocity due to evaporation, with  $m_{evap}$  as the interface evaporation rate,  $\rho_c$  as the density of the condensed phase, and  $\vec{N}$  as the unit normal vector at the interface pointing to the non-condensed phases. We adopt the calculation of  $m_{evap}$  used by a numerical model [27] that was originally derived in Ref. [46].

The transport phenomena in all phases are governed by the conservation of mass, momentum, energy, and chemical species, which can be written respectively as:

$$\frac{\partial \rho}{\partial t} + \nabla \cdot (\rho \vec{V}) = 0, \quad (\text{B.2})$$

$$\begin{aligned} \frac{\partial \rho \vec{V}}{\partial t} + \nabla \cdot (\rho \vec{V} \vec{V}) = & -\nabla p + \nabla \cdot (\mu \nabla \vec{V}) - \frac{\mu}{\kappa} \vec{V} \\ & + \rho_r \vec{g} \beta_T (T - T_r) + \nabla_s T \frac{\partial \gamma}{\partial T} \delta_m(\varphi), \end{aligned} \quad (\text{B.3})$$

$$\frac{\partial \rho h}{\partial t} + \nabla \cdot (\rho \vec{V} h) = \nabla \cdot (k \nabla T), \quad (\text{B.4})$$

$$\frac{\partial \rho Y}{\partial t} + \nabla \cdot (\rho \vec{V} Y) = \nabla \cdot (\rho D \nabla Y). \quad (\text{B.5})$$

In Eqns. B.2-B.5,  $\rho$  is the density,  $\vec{V}$  is the velocity,  $p$  is the pressure,  $\mu$  is the viscosity,  $\kappa$  is the isotropic permeability in the Kozeny-Carman equation,  $\rho_r$  is a reference density at the reference temperature  $T_r$ ,  $\vec{g}$  is the gravitational force vector,  $\beta_T$  is the thermal expansion coefficient,  $T$  is the temperature,  $\nabla_s T$  is the surface gradient of temperature,  $\gamma$  is the surface tension,  $\partial \gamma / \partial T$  is the surface tension coefficient,  $\delta_m(\varphi)$  is the modified delta function,  $h$  is the enthalpy,  $k$  is the thermal conductivity,

$Y$  is the mass fraction of iron vapor in the ambient gas, and  $D$  is the mass diffusivity of iron vapor. Note that the third-through-fifth terms on the right-hand-side (RHS) of Eqn. B.3 represent the dragging force in the mushy region, the thermal-buoyancy force, and the thermal-capillary force, respectively.

At the interface between the condensed and non-condensed phases, a set of jump conditions is enforced as boundary conditions of Eqn. B.2-B.5. We use the notation  $[X]$  to denote the jump between the condensed and non-condensed phases of a physical quantity  $X$ . First, a jump in temperature is enforced according to the theory of the Knudsen layer [47]:

$$[X] = T_c - T_{nc}, \quad (\text{B.6})$$

where  $T_c$  and  $T_{nc}$  are the temperature of the condensed and non-condensed phase at the interface and are calculated according to [47]. The other jump conditions are obtained from the conservation of mass, momentum, and energy across the interface [48]. The mass conservation is written as:

$$[V_N] = m_{evap} \left[ \frac{1}{\rho} \right], \quad (\text{B.7})$$

where  $V_N$  is the velocity normal to the interface. Eqn. B.7 enforces a jump of the velocity normal across the interface that results from evaporation. The momentum conservation is written as:

$$[p] = \gamma K + p_{recoil}(T_c), \quad (\text{B.8})$$

where  $K$  is the curvature of molten pool surface, and  $p_{recoil}$  is the recoil pressure generated by the metal vapor. The term  $p_{recoil}$  is a function of  $T_c$  and is given in Refs. [32, 33]. Eqn. B.8 states that the pressure jump on the LHS is balanced by the summation of capillary force and recoil pressure on the RHS. Finally, the energy conservation is written as:

$$[k \nabla T] = Q_{laser} - \sigma \varepsilon (T^4 - T_\infty^4) - m_{evap} L_{evap}, \quad (\text{B.9})$$

where  $Q_{laser}$  is the power intensity of laser absorption,  $\sigma$  is the Stefan-Boltzmann constant,  $\varepsilon$  is the emissivity,  $T_\infty$  is the ambient temperature, and  $L_{evap}$  is the latent heat of evaporation. The LHS of Eqn. B.9 represents the jump of the conductive heat flux. The three terms on the RHS are the heat fluxes due to laser absorption, radiation, and evaporation, respectively.

The term  $Q_{laser}$  is predicted by a ray-tracing model [32]. The laser is divided into a finite number of rays, each with specific size, position, direction, and power. Upon each incidence of the ray on the keyhole wall, the power of the ray will be partially absorbed by the surface according to the local laser absorptivity  $A$ , and the remainder of the power goes to the reflected rays, with the reflected direction determined by the law of reflection. The keyhole wall is divided into a finite number of segments in the model, and  $Q_{laser}$  for each segment is calculated by dividing the power absorption on each segment by the area of the segment. An example of predicted distribution of  $Q_{laser}$  over the entire keyhole is given in Fig. 4(b). Note that  $A$  is calculated as a function of the laser incident angle,  $\chi$ , according to the Fresnel equation (Eq. B.10).

$$A(\chi) = 1 - \frac{1}{2} \left( \frac{1 + (1 - \varepsilon_c \cos \chi)^2}{1 + (1 + \varepsilon_c \cos \chi)^2} + \frac{\varepsilon_c^2 - 2\varepsilon_c \cos \chi + 2\cos^2 \chi}{\varepsilon_c^2 + 2\varepsilon_c \cos \chi + 2\cos^2 \chi} \right) \quad (\text{B.10})$$

Here  $\epsilon_c$  is a material constant related to its electrical conductance. The laser is assumed unpolarized in this work, so the absorptivity is the average of the P-polarized and S-polarized lasers. The calculated absorptivity is shown by the purple curve in Fig. 8 (b).

All the governing equations are solved using an in-house numerical solver based on the pre-conditioning method [49]. All the boundary conditions are treated with a “sharp interface” method [50]. For all the simulations in this work, the laser parameters and substrate geometry were set to be identical to those in the corresponding subset of DXR experiments, and the physical properties of SS304 were obtained from [32, 33]. The three forces of interest in Table 2, namely the recoil pressure, capillary force, and thermocapillary force, are calculated using the terms  $p_{recoil}$ ,  $\gamma K$ , and  $\nabla_s T \cdot \partial\gamma/\partial T$ , respectively, in Eqns. B.3 and B.8.

## References

- [1] A. Matsunawa, J. Kim, N. Seto, M. Mizutani, and S. Katayama, Dynamics of keyhole and molten pool in laser welding, *J. Laser Appl.* 10(6):247–254 (1998).
- [2] N. P. Calta, J. Wang, A. M. Kiss, A. A. Martin, P. J. Depond, G. M. Guss, V. Thampy, A. Y. Fong, J. Weker, K. H. Stone, C. J. Tassone, M. J. Kramer, M. F. Toney, A. Van Buuren, and M. J. Matthews, An instrument for in situ time-resolved x-ray imaging and diffraction of laser powder bed fusion additive manufacturing processes, *Rev. Sci. Instruments* 89(5):055101 (2018).
- [3] J. Weberpals and F. Dausinger, Fundamental understanding of spatter behavior at laser welding of steel, In *Int. Congress on Appl. Lasers & Electro-Optics 2008*, 704 LIA (2008).
- [4] R. Cunningham, C. Zhao, N. Parab, C. Kantzos, J. Pauza, K. Fezzaa, T. Sun, and A. D. Rollett, Keyhole threshold and morphology in laser melting revealed by ultrahigh-speed x-ray imaging, *Science* 363(6429):849–852 (2019).
- [5] R. Fabbro, Melt pool and keyhole behaviour analysis for deep penetration laser welding, *J. Phys. D. Appl. Phys.* 43(44):445501 (2010).
- [6] R. Fabbro, S. Slimani, F. Coste, and F. Briand, Study of keyhole behaviour for full penetration nd-yag cw laser welding, *J. Phys. D. Appl. Phys.* 38(12):1881 (2005).
- [7] R. Fabbro, S. Slimani, I. Doudet, F. Coste, and F. Briand, Experimental study of the dynamical coupling between the induced vapour plume and the melt pool for nd-yag cw laser welding, *J. Phys. D. Appl. Phys.* 39(2):394 (2006).
- [8] I. Eriksson, J. Powell, and A. F.H. Kaplan, Melt behavior on the keyhole front during high speed laser welding, *Opt. and Lasers in Eng.* 51(6):735–740 (2013).
- [9] Y. Zhang, G. Chen, H. Wei, and J. Zhang, A novel “sandwich” method for observation of the keyhole in deep penetration laser welding, *Opt. and Lasers in Eng.* 46(2):133–139 (2008).
- [10] S. Li, G. Chen, M. Zhang, Y. Zhou, and Y. Zhang, Dynamic keyhole profile during high-power deep-penetration laser welding, *J. Mater. Process Tech.* 214(3):565–570 (2014).
- [11] Y. Zhang, Q. Lin, X. Yin, S. Li, and J. Deng, Experimental research on the dynamic behaviors of the keyhole and molten pool in laser deep-penetration welding, *J. Phys. D. Appl. Phys.* 51(14):145602 (2018).
- [12] F. Fetzer, P. Berger, H. Hu, R. Weber, and T. Graf, Pores in laser beam welding: generation mechanism and impact on the melt flow, In *High-Power Laser Mat Process: Applications, Diagnostics, and Systems VII* 10525, 105250D (2018).
- [13] C. Zhao, K. Fezzaa, R. Cunningham, H. Wen, F. Carlo, L. Chen, A. D. Rollett, and T. Sun, Real-time monitoring of laser powder bed fusion process using high-speed x-ray imaging and diffraction, *Scientific reports* 7(1):3602 (2017).
- [14] L. I. Escano, N. D. Parab, L. Xiong, Q. Guo, C. Zhao, K. Fezzaa, W. Everhart, T. Sun, and L. Chen, Revealing particle-scale powder spreading dynamics in powder-bed-based additive manufacturing process by high-speed x-ray imaging, *Scientific reports* 8(1):15079 (2018).
- [15] N. D. Parab, C. Zhao, R. Cunningham, L. I. Escano, K. Fezzaa, W. Everhart, A. D. Rollett, L. Chen, and T. Sun, Ultrafast x-ray imaging of laser-metal additive manufacturing processes, *J. Synchrotron Radiat.* 25(5) (2018).
- [16] Q. Guo, C. Zhao, L. I. Escano, Z. Young, L. Xiong, K. Fezzaa, W. Everhart, B. Brown, T. Sun, and L. Chen, Transient dynamics of powder spattering in laser powder bed fusion additive manufacturing process revealed by in-situ high-speed high-energy x-ray imaging, *Acta Materialia* 151:169–180 (2018).
- [17] A. A. Martin, N.P. Calta, J. A. Hammons, S. A. Khairallah, M. H. Nielsen, R. M. Shuttlesworth, N. Sinclair, M. J. Matthews, J. R. Jeffries, T. M. Wiley, and J. R. I. Lee, Ultrafast dynamics of laser-metal interactions in additive manufacturing alloys captured by in situ x-ray imaging, *Materials Today Advances* 1:100002 (2019).
- [18] Y. Kawahito, N. Matsumoto, Y. Abe, and S. Katayama, Relationship of laser absorption to keyhole behavior in high power fiber laser welding of stainless steel and aluminum alloy, *J. Mater. Process. Tech.* 211(10):1563–1568 (2011).
- [19] J. Trapp, A. M. Rubenchik, G. Guss, and M. J. Matthews, In situ absorptivity measurements of metallic powders during laser powder-bed fusion additive manufacturing, *Appl. Mater. Today* 9:341–349 (2017).
- [20] B. J. Simonds, J. W. Sowards, J. Hadler, E. Pfeif, B. Wilthan, J. Tanner, C. Harris, P. A. Williams, and J. Lehman, Dynamic and absolute measurements of laser coupling efficiency during laser spot welds, *Procedia CIRP* 74:632–635 (2018).
- [21] H. Ki, P. S. Mohanty, and J. Mazumder, Multiple reflection and its influence on keyhole evolution, In *Int. Congress on Appl. Lasers & Electro-Optics 2001*, 933–942. LIA (2001).
- [22] J. Cho and S. Na, Implementation of real-time multiple reflection and Fresnel absorption of laser beam in keyhole, *J. Phys. D. Appl. Phys.* 39(24):5372 (2006).
- [23] A. Kar, T. Rockstroh, and J. Mazumder, Two-dimensional model for laser-induced materials damage: Effects of assist gas and multiple reflections inside the cavity, *J. Appl. Phys.* 71(6):2560–2569 (1992).
- [24] J. Milewski and E. Sklar, Modelling and validation of multiple reflections for enhanced laser welding, *Model. and Simul. in Mater. Sci. and Eng.* 4(3):305 (1996).
- [25] P. Solana and G. Negro, A study of the effect of multiple reflections on the shape of the keyhole in the laser processing of materials, *J. Phys. D. Appl. Phys.* 30(23):3216 (1997).
- [26] P.S. Wei and C.Y. Ho, Beam focusing characteristics effect on energy reflection and absorption in a drilling or welding cavity of paraboloid of revolution, *Int. J. heat and mass transfer* 41(21):3299–3308 (1998).
- [27] H. Ki, J. Mazumder, and P. S. Mohanty, Modeling of laser keyhole welding: Part i. mathematical modeling, numerical methodology, role of recoil pressure, multiple reflections, and free surface evolution, *Metallurgical and materials transactions A* 33(6):1817–1830 (2002).
- [28] J. Lee, S. H. Ko, D. F. Farson, and C. D. Yoo, Mechanism of keyhole formation and stability in stationary laser welding *J. Phys. D. Appl. Phys.* 35(13):1570 (2002).
- [29] J. Zhou, H. Tsai, and P. Wang, Transport phenomena and keyhole dynamics during pulsed laser welding, *J. Heat Trans.* 128(7):680–690 (2006).
- [30] S. Pang, L. Chen, J. Zhou, Y. Yin, and T. Chen, A three-dimensional sharp interface model for self-consistent keyhole and weld pool dynamics in deep penetration laser welding, *J. Phys. D. Appl. Phys.* 44(2):025301 (2010).
- [31] H. Zhao, W. Niu, B. Zhang, Y. Lei, M. Kodama, and T. Ishide, Modelling of keyhole dynamics and porosity formation considering the adaptive keyhole shape and three-phase coupling during deep-penetration laser welding, *J. Phys. D. Appl. Phys.* 44(48):485302 (2011).
- [32] W. Tan, N. S. Bailey, and Y. C. Shin, Investigation of keyhole plume and molten pool based on a three-dimensional dynamic model with sharp interface formulation, *J. Phys. D. Appl. Phys.* 46(5):055501 (2013).
- [33] W. Tan and Y. C. Shin, Analysis of multi-phase interaction and its effects on keyhole dynamics with a multi-physics numerical model, *J. Phys. D. Appl. Phys.* 47(34):345501 (2014).
- [34] M. Courtois, M. Carin, P. Le Masson, S. Gaied, and M. Balabane, A complete model of keyhole and melt pool dynamics to analyze instabilities and collapse during laser welding, *J. Laser Appl.* 26(4):042001 (2014).

- [35] S. A. Khairallah and A. Anderson, Mesoscopic simulation model of selective laser melting of stainless steel powder, *J. of Mater. Process. Tech.* 214(11):2627–2636 (2014).
- [36] S. A. Khairallah, A. T. Anderson, A. Rubenchik, and W. E. King, Laser powder-bed fusion additive manufacturing: Physics of complex melt flow and formation mechanisms of pores, spatter, and denudation zones, *Acta Materialia* 108:36–45 (2016).
- [37] Y. Ai, P. Jiang, X. Shao, P. Li, and C. Wang, A three-dimensional numerical simulation model for weld characteristics analysis in fiber laser keyhole welding, *Int. J. of Heat and Mass Transfer* 108:614–626 (2017).
- [38] C. Panwisawas, B. Perumal, R. M. Ward, N. Turner, R. P. Turner, J. W. Brooks, and H. C. Basoalto, Keyhole formation and thermal fluid flow-induced porosity during laser fusion welding in titanium alloys: Experimental and modelling, *Acta Materialia* 126:251–263 (2017).
- [39] W. Yan, Y. Qian, W. Ge, S. Lin, W. Liu, F. Lin, and G. J. Wagner, Mesoscale modeling of multiple-layer fabrication process in selective electron beam melting: inter-layer/track voids formation, *Materials & Design*, 141:210–219 (2018).
- [40] D. Farson, K. Hillsley, J. Sames, and R. Young, Frequency–time characteristics of air-borne signals from laser welds, *J. Laser Appl.* 8(1):33–42 (1996).
- [41] A. Matsunawa, J. Kim, S. Katayama, and V. V. Semak, Experimental and theoretical studies on keyhole dynamics in laser welding, In *Int. Congress on Applications of Lasers & Electro-Optics 1996*, B58–B67 LIA (1996).
- [42] S. Ao, Z. Luo, M. Feng, and F. Yan, Simulation and experimental analysis of acoustic signal characteristics in laser welding, *The Int. J. of Adv. Manu. Tech.* 81(1-4):277–287 (2015).
- [43] R. Fabbro, M. Dal, P. Peyre, F. Coste, M. Schneider, and V. Gunenthiram, Analysis and possible estimation of keyhole depths evolution, using laser operating parameters and material properties, *J. Laser Appl.* 30(3):032410, (2018).
- [44] R. Fabbro, Scaling laws for the laser welding process in keyhole mode, *J. of Mater. Process. Tech.* 264:346–351 (2019).
- [45] S. Osher and R. Fedkiw, Level set methods and dynamic implicit surfaces, *Springer Science & Business Media* 44:77 (2002).
- [46] T. Ytrehus and S. Østmo, Kinetic theory approach to interphase processes, *Int. J. Multiphase Flow* 22(1):133–155 (1996).
- [47] C. J. Knight, Theoretical modeling of rapid surface vaporization with back pressure, *AIAA J.* 17(5):519–523 (1979).
- [48] F. Gibou, L. Chen, D. Nguyen, and S. Banerjee, A level set based sharp interface method for the multiphase incompressible navier–stokes equations with phase change, *J. Comput. Phys* 222(2):536–555 (2007).
- [49] D. Li and C. L. Merkle, A unified framework for incompressible and compressible fluid flows, *J. of hydrodynamics* 18(1):111–117 (2006).
- [50] R. P. Fedkiw, T. Aslam, B. Merriman, and S. Osher, A non-oscillatory eulerian approach to interfaces in multimaterial flows (the ghost fluid method), *J. Comput. Phys.* 152(2):457–492 (1999).